JACS
JOURNAL OF THE AMERICAN CHEMICAL SOCIETY
pubs.acs.org/JACS
Article

Selective Mass Accumulation at the Metal–Polymer Bridging Interface for Efficient Nitrate Electroreduction to Ammonia and Zn-Nitrate Batteries

Guojie Chao,[#] Wei Zong,[*,#] Jiexin Zhu,[#] Haifeng Wang,[#] Kaibin Chu, Hele Guo, Jian Wang, Yuhang Dai, Xuan Gao, Longxiang Liu, Fei Guo, Ivan P. Parkin, Wei Luo, Paul R. Shearing, Longsheng Zhang,[*] Guanjie He,[*] and Tianxi Liu[*]

Cite This: J. Am. Chem. Soc. 2025, 147, 21432–21442

Read Online

ACCESS | Metrics & More | Article Recommendations | Supporting Information

ABSTRACT: The electrochemical conversion of nitrate (NO_3^-), a common nitrogen source in industrial wastewater and contaminated groundwater, into ammonia (NH_3), signifies an approach to wastewater treatment and NH_3 production. Nevertheless, its selectivity and activity at low NO_3^- concentrations and industrial current densities are constrained by limited mass transfer around the electrode. Here, we report a metal–polymer bridging interface constructed by anchoring Cu/Cu_2O nanoparticles onto a two-dimensional (2D) Cu-based benzene dicarboxylate (CuBDC) coordination polymer via in situ electroreduction (denoted as E-CuBDC). This interface weakens the electrostatic repulsion and regulates the distribution/migration of NO_3^- and H_2O, creating a Janus NO_3^--rich and H_2O-poor domain near the catalyst surface. Operando characterizations and theoretical simulations indicate that the metal–polymer bridging interface selectively accumulates NO_3^- and reduces the energy barrier toward the reduction of $*NH_2OH$ to $*NH_2$, overcoming the mass transfer limitations at a low NO_3^- concentration. E-CuBDC exhibits a high Faradaic efficiency (FE) of over 90% across wide NO_3^- concentrations (7.1–100 mM NO_3^-) and high applied voltages. Additionally, it achieved stable NH_3 production over 100 h at ampere-level current densities. When applied in a Zn–NO_3^- system, this newly developed E-CuBDC catalyst demonstrates an outstanding power density and FE for NH_3 production, showcasing its great potential for large-scale electrochemical conversion and storage systems. This study presents a generalizable strategy for constructing metal–polymer interfaces to regulate interfacial mass transport.

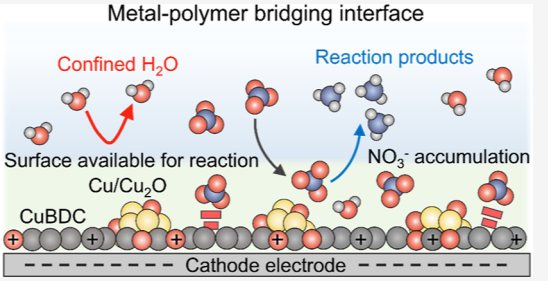

INTRODUCTION

Ammonia (NH_3) is one of the most widely utilized fundamental chemicals across numerous industries, including the fields of textiles, agriculture, and plastics, serving as the high-energy-density carrier for renewable hydrogen storage and utilization.[1−4] Compared to chemically inert nitrogen (N_2), NH_3 is a more reactive and readily utilizable nitrogen source, thereby increasing the economic viability and practical applicability of nitrogen-based processes.[5,6] In recent years, industrial-scale NH_3 production by the Haber–Bosch method has succeeded in providing affordable fertilizers for supporting the NH_3 industry and feeding the population. However, the energy-intensive NH_3 synthesis method has led to high energy consumption and greenhouse gas emissions.[7−10] Significant efforts have been directed toward developing innovative methods for green and sustainable NH_3 electrosynthesis to reduce reliance on fossil fuels and mitigate environmental pollution. Electrochemical nitrate (NO_3^-) reduction reaction (NITRR) is an emerging technology that provides a more sustainable pathway process for NH_3 production.[11−14] Moreover, NO_3^-, commonly found as a water contaminant in nature owing to agricultural runoff and industrial wastewater discharge, is ubiquitous in the environment, leading to water pollution and human health hazards.[15] NITRR not only serves as an operational tool for restoring the disrupted nitrogen cycle and expediting wastewater denitrification but also offers an eco-conscious and sustainable method for NH_3 production.[16,17] Nevertheless, the development of electrocatalysts with both high activity and high selectivity for NITRR poses a formidable challenge. Currently, Cu-based catalysts are regarded as promising candidates for NITRR due to their favorable ability to activate NO_3^-.[18−21]

Received: January 8, 2025
Revised: May 31, 2025
Accepted: June 2, 2025
Published: June 11, 2025

https://doi.org/10.1021/jacs.5c00400
J. Am. Chem. Soc. 2025, 147, 21432–21442

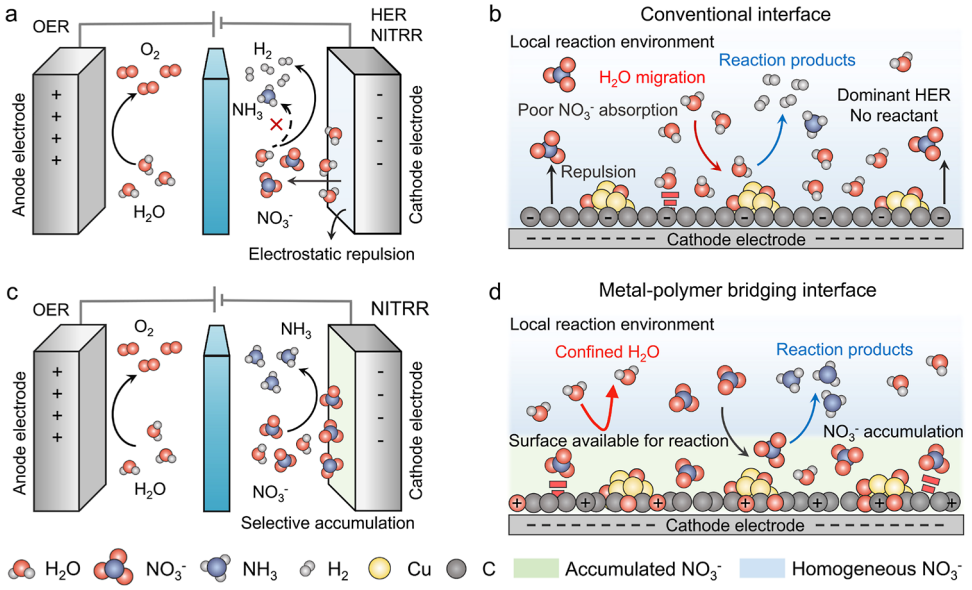

Figure 1. Schematics for the mass transport at the conventional and metal−polymer bridging interfaces. (a,b) Schematics illustrating the unregulated H_2O and NO_3^- mass transport at the conventional interface in the OER||NITRR electrolyzer. Random H_2O migration and NO_3^- expulsion occur in the local reaction environment near the cathode electrode, where electrostatic repulsion inhibits the access of NO_3^- to the catalyst surface, favoring the HER over NITRR. (c,d) Schematics illustrating the controlled H_2O and NO_3^- mass transport at the metal−polymer bridging interface in the OER||NITRR electrolyzer. Confined H_2O migration and NO_3^- accumulation occur in the local reaction environment near the cathode electrode, favoring the NITRR over HER. Red ball represents the O atom, gray ball represents the H atom, dark gray ball represents the C atom, and dark blue ball represents the N atom. HER signifies the hydrogen evolution reaction, and OER signifies the oxygen evolution reaction.

For instance, Zhang et al.[18] reported that CuO NWAs are beneficial to the formation of *NOH reaction intermediate and exhibit a high energy barrier of H_2 formation, resulting in an enhanced selectivity for NO_3^- reduction to NH_3. Despite the progress made thus far, however, one of the persistent bottlenecks is the electrostatic repulsion occurring at the electrode−electrolyte interface, which hampers the mass transfer process of NO_3^- and leads to a sharp decline in the concentration of NO_3^- in the vicinity of electrode interfaces (Figure 1a).[22−24] As a representative interface reaction, NITRR mainly comprises two fundamental stages: adsorption and catalysis, in which the initiation of NITRR relies on effective NO_3^- adsorption, making it a crucial factor in surmounting the limitations associated with the low binding affinity of NO_3^- reactants. Besides, the catalyst surface is predominantly occupied by water molecules, which favors the competing hydrogen evolution reaction (HER),[25−27] leading to poor Faradaic efficiency (FE) and NH_3 yield of NITRR (Figure 1b). This situation is further exacerbated by NITRR electrocatalysis in real wastewater treatment, including conditions of low concentration and industrial-scale current. To effectively and selectively promote NITRR, modulating the mass transfer near the electrode region could be a feasible approach to overcoming the challenges mentioned above.[28−30] A microenvironment modulation that breaks the mass transfer restriction of NO_3^- in the proximity of the catalyst surface might efficiently promote NITRR performance. Although the microenvironment is expected to play a significant role, assessing the extent of its impact on reaction processes remains highly challenging. Specifically, it is crucial to deeply investigate the relationship between the interface microenvironment and its influence on tailoring NITRR activity and selectivity.

In this work, we report a Janus metal−polymer bridging interface that enriches NO_3^- and blocks H_2O, enabling efficient electrochemical NH_3 production from NO_3^- across wide concentrations and at ampere-level current densities. This Janus interface is constructed by bridging Cu/Cu_2O nanoparticles (NPs) onto a Cu-based benzene dicarboxylate (CuBDC) coordination polymer via an in situ electroreduction method. For the as-formed catalyst (denoted as E-CuBDC), a series of operando characterizations combined with theoretical simulations reveals that the metal−polymer bridging interface weakens electrostatic repulsion near the catalyst surface, thereby facilitating NO_3^- mass transfer and confining H_2O accessibility. Moreover, the metal−polymer interface enhances the adsorption of NO_3^- and reduces the energy barrier of the step (*NH_2OH to *NH_2). The regulated distribution and migration of NO_3^- and H_2O create a NO_3^--rich and H_2O-poor domain near the catalyst surface. This affords the catalyst a kinetically favorable local environment for promoting NITRR and alleviating HER (Figure 1c,d). As a result, E-CuBDC achieves an exceptional FE over 90% across the NITRR electrocatalysis with NO_3^- concentrations ranging from 7.1 to 100 mM and a high NH_3 yield rate of 77.9 mg h^{-1} cm^{-2} at a current density of ~1.2 A cm^{-2} in a flow cell. The performance evaluation in the Zn−NO_3^- cell demonstrates a power density of 17.9 mW cm^{-2} and a FE of 82.2% for NH_3 production.

RESULTS AND DISCUSSION

To explore the feasibility of the metal−polymer bridging interface design, we first synthesized CuBDC via an interfacial reaction method at room temperature (Figure S1). To modulate the catalyst structure, various CuBDC-*x* samples (denoted as CuBDC-1, CuBDC, and CuBDC-2) were synthesized through adjusting the molar ratios (1:1, 2:1, and 4:1) of copper acetate and 1,4-benzenedicarboxylic acid (TA).

https://doi.org/10.1021/jacs.5c00400
J. Am. Chem. Soc. 2025, 147, 21432−21442

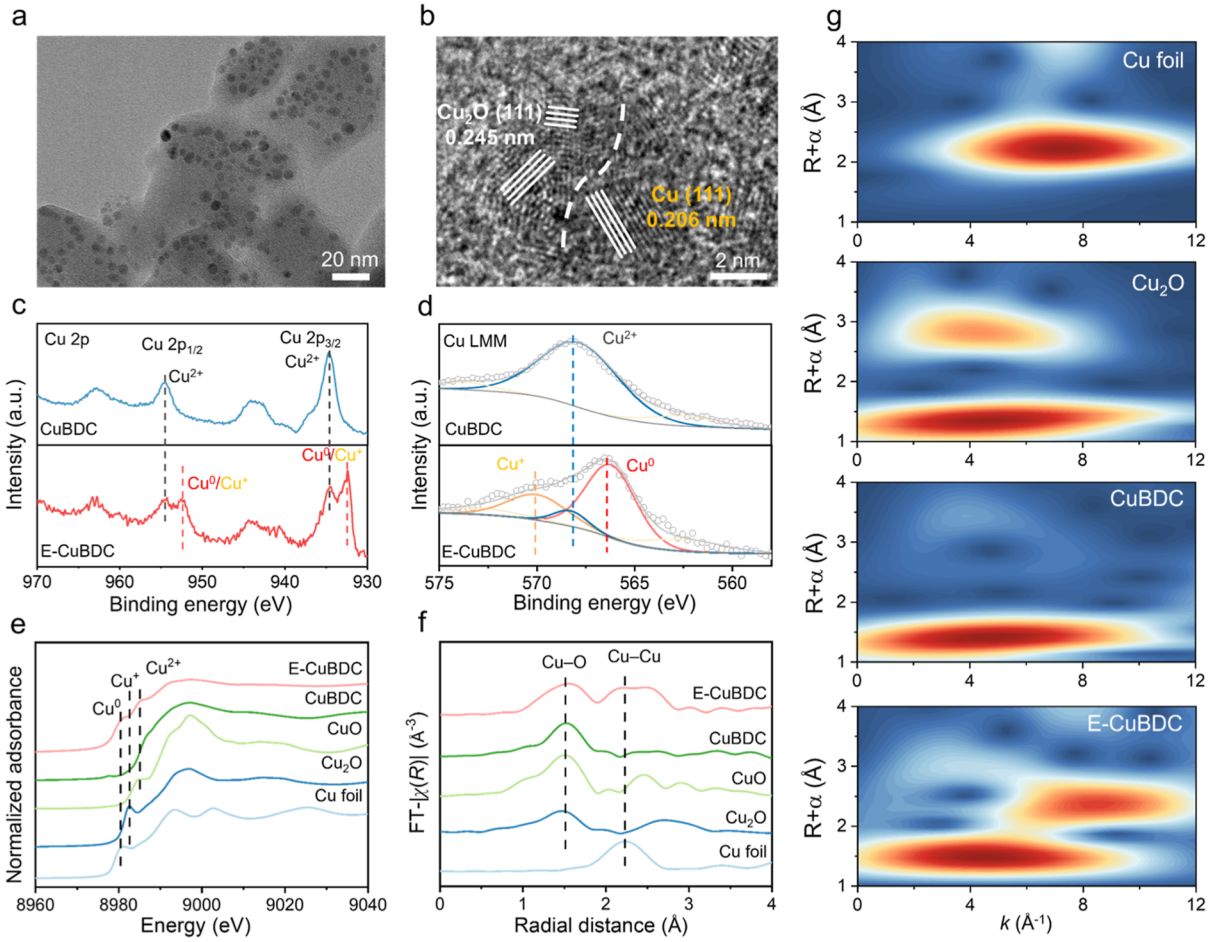

Figure 2. Materials synthesis and characterization. (a,b) Low- and high-magnification TEM images of E-CuBDC, respectively. (c) High-resolution Cu 2p X-ray photoelectron spectroscopy (XPS) and (d) Cu LMM Auger electron spectra of CuBDC and E-CuBDC. (e) Cu K-edge synchrotron radiation X-ray absorption near-edge structure (SR-XANES) and (f) synchrotron radiation extended X-ray absorption fine structure (SR-EXAFS) spectra of E-CuBDC, CuBDC, CuO, Cu_2O, and Cu foil, respectively. (g) Wavelet transform analysis of E-CuBDC, CuBDC, Cu_2O, and Cu foil.

The catalyst with a balanced Cu/TA molar ratio of 2:1 was designated as CuBDC and served as a reference. The coordination bonds between the inorganic nodes and organic linker in CuBDC were first characterized by Fourier transform infrared (FTIR) spectroscopy. Two peaks of −COO− are observed at 1570 and 1397 cm^{-1} for TA and CuBDC-*x* samples, which were attributed to the asymmetric and symmetric vibrations of the −COO− group (Figure S2).[31] A typical C−O−Cu stretching vibration peak at around 1091 cm^{-1} is observed. In sharp contrast to TA, the carbonyl peak associated with the protonated carboxyl group disappears in CuBDC-*x* samples within the range of 1710−1760 cm^{-1}, indicative of coordination between Cu^{2+} and the carboxyl group. The crystalline structures of CuBDC-*x* samples were further validated by X-ray diffraction (XRD) and transmission electron microscopy (TEM). Indeed, Figure S3 shows that different CuBDC-*x* samples display similar diffraction peaks to those reported in the previous literature studies,[32,33] indicating the preparation of crystalline CuBDC-*x*. As shown in Figure S4 from TEM images, CuBDC exhibits a well-defined 2D flaky structure with discernible lattice fringes, confirming its crystallinity. The CuBDC-*x* samples were utilized as catalysts following an electrochemical activation approach, which involved electrochemically reducing CuBDC in a 1 M KOH−0.1 M NO_3^--N electrolyte to produce the E-CuBDC catalyst. Then, a series of characterizations were employed to elucidate the structural evolution and reaction mechanism of E-CuBDC. As displayed in Figures 2a and S5a, the TEM images of E-CuBDC demonstrate the uniform distribution of small bright clusters, each with a diameter of about 4−8 nm on the CuBDC surface, which arises from the electrochemical reduction of the Cu−O nodes in CuBDC. In the high-resolution TEM image of E-CuBDC (Figures 2b and S5b), twin lattice fringes with spacings of 0.206 and 0.245 nm were observed, corresponding to the Cu (111) and Cu_2O (111) planes. Moreover, the high-angle annular dark-field scanning TEM image, coupled with X-ray energy-dispersive spectroscopy mapping images, further validates the spatial overlap of C, O, and Cu elements, highlighting the coexistence of Cu/Cu_2O NPs and CuBDC (Figure S6).

This uniform distribution ensures effective interactions between the Cu/Cu_2O NPs and CuBDC. Meanwhile, the formation of Cu and Cu_2O species was verified through XRD (Figure S7) and Raman spectra (Figure S8).[34] As shown in Figure S9, FTIR spectroscopy of E-CuBDC displays characteristic peaks at around 1570, 1397, and 1091 cm^{-1}, corresponding to the antisymmetric and symmetric stretching vibration of the −COO− group and the C−O−Cu stretching vibration.[31,32] The chemical components and valence states of the E-CuBDC and CuBDC were further investigated by XPS.

https://doi.org/10.1021/jacs.5c00400
J. Am. Chem. Soc. 2025, 147, 21432−21442

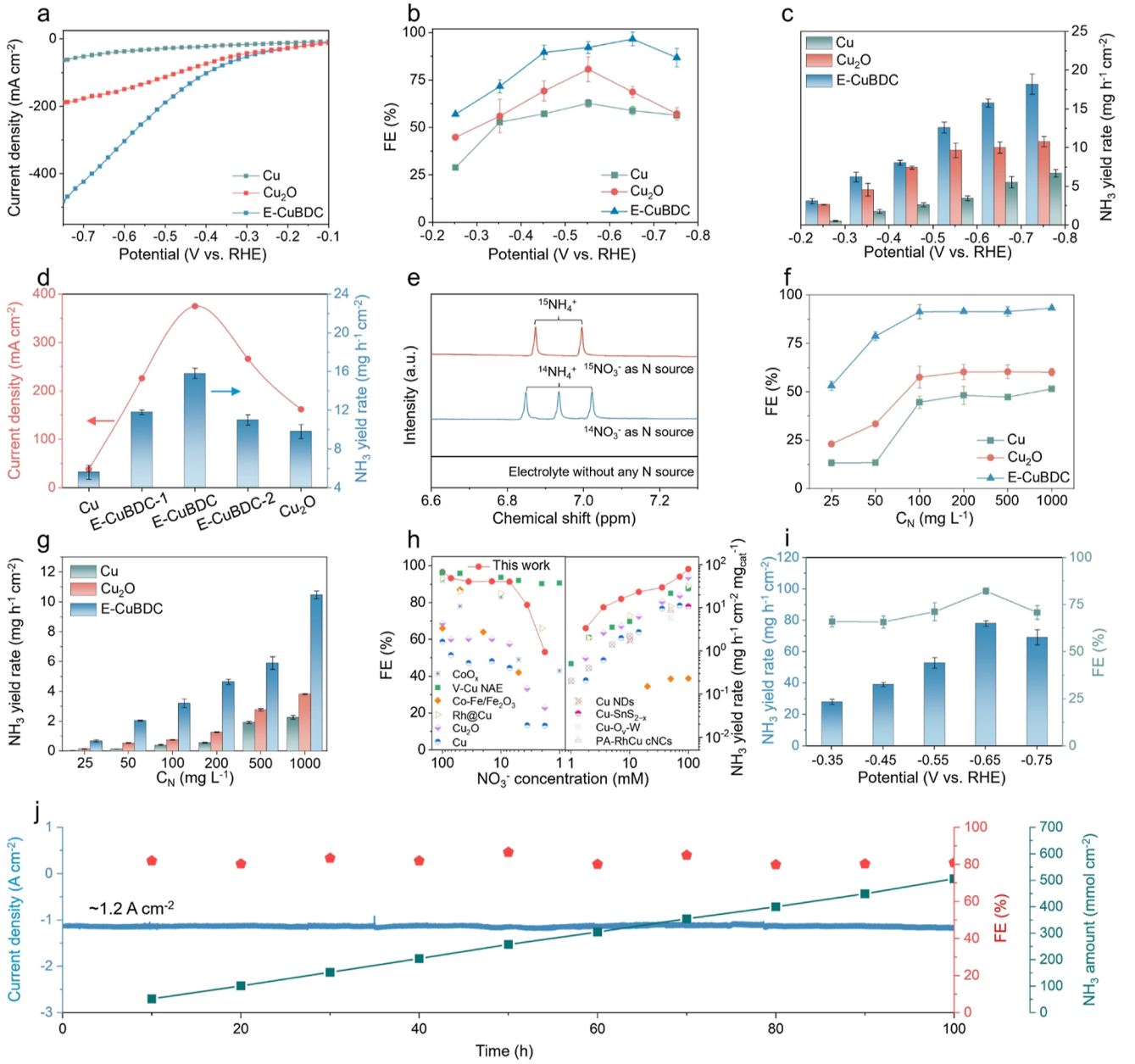

Figure 3. Electrochemical NITRR performance. (a) LSV curves of E-CuBDC, Cu_2O, and Cu. (b,c) FE_{NH_3} and NH_3 yield rate of E-CuBDC, Cu_2O, and Cu at various potentials, respectively. (d) j_{NH_3} and NH_3 yield rate for E-CuBDC-*x* with different Cu/TA ratios, Cu_2O, and Cu. (e) ^1H NMR spectra for the N-isotope labeling experiments of E-CuBDC. (f,g) FE_{NH_3} and NH_3 yield rate of E-CuBDC with various NO_3^--N concentrations from 25 to 1000 mg L^{-1}, respectively. (h) Comparison of the NITRR performance between E-CuBDC and other previously reported electrocatalysts. (i) NH_3 yield rate and FE_{NH_3} of E-CuBDC@Ni foam at various potentials. (j) Total NH_3 amount and FE_{NH_3} of E-CuBDC@Ni foam in the stability experiment at −0.65 V vs RHE.

Compared to CuBDC, two new peaks at 932.4 and 952.5 eV were observed in the high-resolution Cu 2p spectra of E-CuBDC (Figure 2c), which are associated with the Cu^0/Cu^+ species. Meanwhile, as shown in the Cu LMM Auger electron spectroscopy of E-CuBDC (Figure 2d), three characteristic peaks at binding energies of 570.1, 568.3, and 566.4 eV can be attributed to Cu^+, Cu^{2+}, and Cu^0 species, respectively, confirming the formation of Cu/Cu_2O NPs on the surface of CuBDC.[35−37] Collectively, the above results demonstrate that the Cu/Cu_2O NPs are introduced on the surface of CuBDC during the electrochemical reduction. The local structural characterization of Cu species was conducted through SR-XANES spectroscopy, utilizing CuO, Cu_2O, and Cu foil as comparative references (Figure 2e). It can be found that the absorption near-edge position of CuBDC closely resembles that of the CuO reference, suggesting that its valence state is mainly Cu^{2+}. In contrast, the SR-XANES Cu K-edge of E-CuBDC shifts toward low energy and displays characteristic peaks of Cu^+ and Cu^0 species. The SR-EXAFS spectra of CuBDC and E-CuBDC show an obvious peak at 1.5 Å assigned to the Cu−O scattering path (Figure 2f). Moreover, E-CuBDC exhibits a new peak located at ∼2.2 Å that originates from the scattering paths of the Cu−Cu bonds, demonstrating the formation of Cu^0 in E-CuBDC.[38]

https://doi.org/10.1021/jacs.5c00400
J. Am. Chem. Soc. 2025, 147, 21432−21442

Furthermore, the structural reconstruction of the Cu species in E-CuBDC is corroborated by the wavelet transform analysis of SR-EXAFS spectra (Figure 2g). E-CuBDC shows an intensity maximum of about 4.5 $Å^{-1}$ from the Cu−O bond, similar to that observed in CuBDC. The weak intensity at ∼8.3 $Å^{-1}$ corresponding to the Cu−Cu bond is slightly higher than that of Cu foil (∼7.8 $Å^{-1}$). The combined results above demonstrate that CuBDC underwent self-adaptive reconstruction during the NITRR process, which was transformed into E-CuBDC with superficially emended Cu/Cu_2O NPs. The above result demonstrates that the metal−polymer interface was successfully constructed during the NITRR process (Figure S10 and Note S1).

To further seek experimental evidence for metal−polymer interface design, we evaluated the electrocatalytic performance of as-prepared catalysts toward NITRR in a customized H-cell under ambient conditions. As depicted in Figure S11, the linear sweep voltammetry (LSV) curves of E-CuBDC-*x* were recorded in a 1 M KOH solution with and without 0.1 M NO_3^--N, respectively. The current density of the LSV curves shows a marked increase with the addition of NO_3^- to the electrolyte, indicating the initiation of the NITRR process. In comparison to the commercial Cu and Cu_2O samples (Figure 3a), E-CuBDC shows an enhanced geometrically normalized current density (j_{NH_3}) of the NITRR process, and the highest j_{NH_3} of E-CuBDC indicates its superior catalytic activity for NITRR. The corresponding Tafel slope derived from the LSV curves for E-CuBDC was 341 mV dec^{-1}, which was lower than other control samples (E-CuBDC-1 and E-CuBDC-2), Cu, and Cu_2O catalysts (Figures S12 and S13). These above results imply that E-CuBDC exhibits improved reaction kinetics at the electrolyte−catalyst interface during the NITRR process. The NITRR performance was then determined by chronoamperometry (*i*−*t*) tests at various potentials ranging from −0.25 to −0.75 V vs reversible hydrogen electrode (RHE), as shown in Figure S14. Detection of NH_3 and NO_2^- production in electrolytes was carried out using an ultraviolet−visible spectrophotometer (Figure S15). As illustrated in Figure 3b,c, the NH_3 yield rate of E-CuBDC progressively increased, and the corresponding NH_3 Faradaic efficiency (FE_{NH_3}) shows a volcanic shape. E-CuBDC reached a maximum of 96.6% at −0.65 V vs RHE, with an NH_3 yield rate of 15.7 mg h^{-1} cm^{-2}, in which the NH_3 yield rate was approximately 1.5 times and 2.8 times than that of Cu_2O and Cu reference, respectively. It was observed that both more positive and more negative potentials lead to a decrease in FE_{NH_3}. This decline is attributed to two distinct factors: at more positive potentials, the insufficient supply of *H results in a less efficient *NO_2 deoxygenation−hydrogenation process, while at more negative potentials, intensified competition from the HER process becomes dominant. Moreover, the continuous increase in NH_3 yield rate is attributed to the abundant generation of *H, which promotes the hydrogenation steps toward NH_3 production.[13,39] In contrast, E-CuBDC can maintain higher FE_{NH_3} values at more negative potentials, such as 86.8% for E-CuBDC, 57.2% for Cu_2O, and 56.5% for Cu at −0.75 V vs RHE.

To elucidate the effect of Cu content on the NITRR performance, E-CuBDC-*x* catalysts with varying Cu/TA ratios were synthesized and tested. As shown in Figure 3d, with the increase of Cu/TA ratios, both j_{NH_3} and NH_3 yield rates display noteworthy enhancements. A distinctive volcano-shaped trend is observed between the j_{NH_3} and the NH_3 yield rate, reaching its peak on E-CuBDC, with the highest values of 364 mA cm^{-2} and 15.7 mg h^{-1} cm^{-2}. This exceeded those of E-CuBDC-1 (i.e., 226 mA cm^{-2} and 11.7 mg h^{-1} cm^{-2}) and E-CuBDC-2 catalysts (i.e., 266 mA cm^{-2} and 11.0 mg h^{-1} cm^{-2}), as depicted in Figure S17. The j_{NH_3} and NH_3 yield rates declined dramatically when the Cu/TA ratios exceeded 2. Therefore, maintaining a balanced Cu/TA ratio is crucial for sustaining the optimal catalytic performance in ammonia production. Furthermore, the electrochemically active surface area (ECSA) was measured in the nonfaradaic reaction range. E-CuBDC shows higher ECSA values than the other E-CuBDC-*x*, Cu, and Cu_2O owing to the increased electro-active surface area. This corroborates its highest intrinsic activity for NH_3 synthesis (Figures S18 and S19). Isotope labeling experiments were also conducted to confirm the nitrogen source of synthesized NH_4^+. Figure 3e presents the ^1H NMR spectra of the electrolyte following NITRR tests, labeled with the ^{15}N isotope, wherein characteristic double peaks of $^{15}NH_4^+$ at δ = 6.87 and 6.99 ppm were observed. These results suggest that produced NH_3 originates entirely from NO_3^- electroreduction.

To research the practicability potential, a series of experiments were performed. Considering the variability of the NO_3^- levels in wastewater at different scenarios, it is imperative for the catalyst to demonstrate robust performance across a broad range of NO_3^- concentrations. Therefore, we simulated the degradation of waste streams (e.g., textile and industrial wastewater) with NO_3^--N concentrations ranging from 25 to 1000 NO_3^--N mg L^{-1}. As demonstrated in Figure 3f,g, E-CuBDC exhibits a FE_{NH_3} of 91.3% with a NO_3^--N concentration of 100 mg L^{-1} (7.1 mM NO_3^- concentration) and maintains FE_{NH_3} over 90% in the NO_3^--N concentrations range from 100 to 1000 NO_3^--N mg L^{-1}. In contrast, Cu and Cu_2O consistently lagged behind E-CuBDC in the NH_3 yield rate and FE_{NH_3} across a wide range of concentrations. E-CuBDC exhibited a comparable NH_3 yield rate and FE_{NH_3} at a NO_3^--N concentration of 25 mg L^{-1}, almost equivalent to the performance of Cu and Cu_2O at a NO_3^--N concentration of 100 mg L^{-1}. This distinction validates the effect of the Cu/Cu_2O−CuBDC interface in promoting NO_3^- mass transfer, especially in low concentrations of NO_3^-. As presented in Figure 3h, the NH_3 yield rate and the FE_{NH_3} of E-CuBDC are on par with those of the other reported catalysts for NITRR within the NO_3^- concentration range of 25−1400 NO_3^--N mg L^{-1} (1.78−100 mM NO_3^- concentration, Tables S1 and S2). Meanwhile, under higher NO_3^- concentrations (above 0.1 M) and neutral conditions, E-CuBDC still maintains high NH_3 production with FE_{NH_3} over 90% (Figures S20 and S21).

The stability at industrially relevant current densities is a key requisite for practical applications. Further, we prepared working electrodes by spreading E-CuBDC ink on Ni foam (E-CuBDC@Ni foam) to simulate industrial applications, given the relatively inert activity of Ni for the NITRR. The Ni foam was commonly selected as a self-supporting substrate for nanostructured electrocatalysts due to its cost-effectiveness and superior electrical conductivity. In the illustrated LSV curves within the potential range from −0.35 to −0.75 V, E-CuBDC exhibits an ampere-level current density markedly surpassing that of the Ni foam (Figures S22 and S23). This indicates Ni

https://doi.org/10.1021/jacs.5c00400
J. Am. Chem. Soc. 2025, 147, 21432−21442

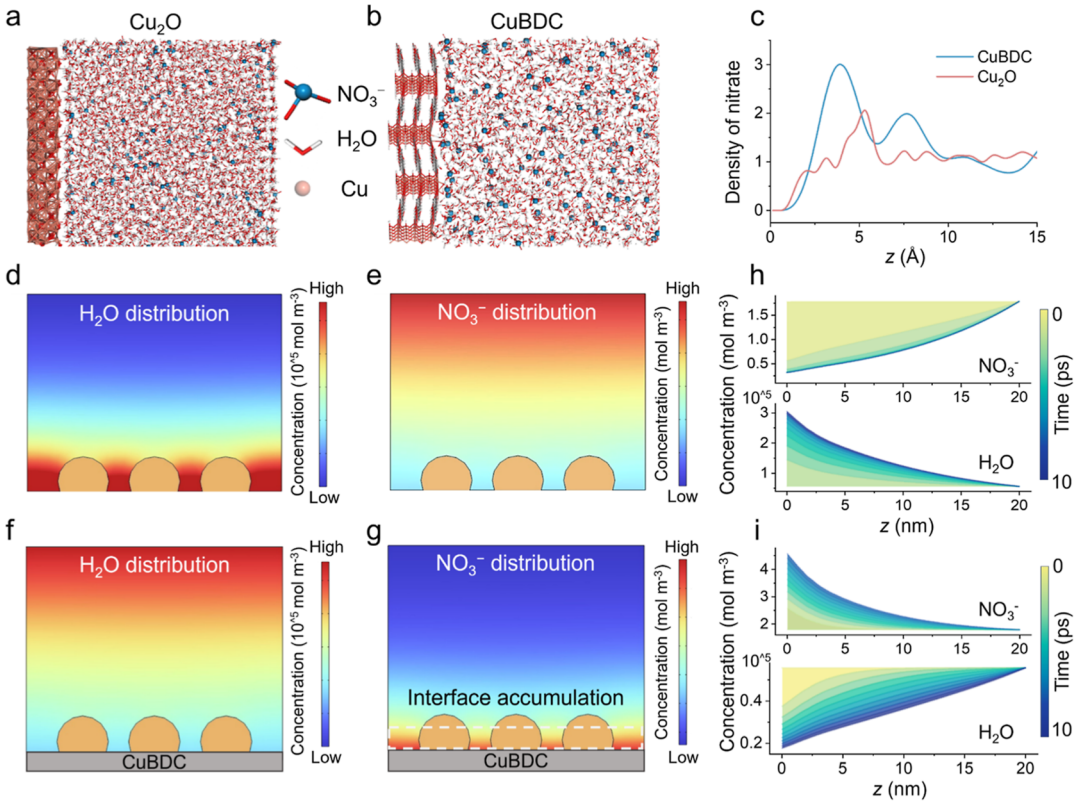

Figure 4. Molecular dynamics and COMSOL Multiphysics simulations. (a,b) Snapshots of the interfacial structures of Cu_2O and CuBDC models from molecular dynamics simulations, respectively. (c) Corresponding interfacial accumulated density of NO_3^- for the CuBDC and Cu_2O models. (d,e) Distributions of H_2O and NO_3^- at 10 ps for the Cu_2O model. (f,g) Distributions of H_2O and NO_3^- for the E-CuBDC model at 10 ps. (h,i) The concentrations of H_2O and NO_3^- as a function of distance from the catalyst surface for Cu/Cu_2O and E-CuBDC at various times.

foam exhibits no discernible impact on the NITRR process, aligning with previously reported findings.[40−43] Notably, E-CuBDC achieves a high NH_3 yield rate of 77.9 mg h^{-1} cm^{-2}, with the highest FE_{NH_3} of 82.1% at −0.65 V vs RHE (Figure 3i). The stability test with continuous electrolyte flow demonstrated sustained current density at ∼1.2 A cm^{-2} over 100 h (Figure 3j). These results demonstrated the excellent performance of E-CuBDC across a broad range of NO_3^- concentrations and ampere-level currents, providing a promising avenue for addressing the intricate challenges posed by NO_3^--containing wastewater in industrial applications.

To study the function of CuBDC at the metal−polymer interface, we examined the NO_3^- management by conducting molecular dynamics simulations to study the distribution/migration of NO_3^- near the Cu_2O and CuBDC surface. The initial configurations in the simulation boxes were established by randomly distributing the NO_3^- and H_2O with Cu_2O and the CuBDC layer. In the constructed model, the direction from left to right is defined as the *Z*-direction (Figure 4a,b). Of note is that there is a higher NO_3^- concentration near the surface of the CuBDC model compared to the Cu_2O model (Figure 4c). This indicates that CuBDC can offer anchoring sites to trigger the interfacial accumulation of NO_3^-. Additionally, we found that CuBDC, functioning as a support, can modulate the surface potential. As depicted in Figure S24, the surface zeta potential of CuBDC is determined to be 3.95 ± 0.67 mV, compared with those of Cu_2O (−12.16 ± 1.15 mV) and Cu (−16.07 ± 0.51 mV). The relatively positive surface potential of CuBDC is conducive to the adsorption and enrichment of NO_3^-. Hence, the construction of the NITRR catalysts with a more positive surface potential may facilitate overcoming poor mass transfer and low-concentration gradients in the vicinity of the catalyst domain. Furthermore, we tracked changes in NO_3^- and H_2O concentrations around the catalyst surface of Cu/Cu_2O and E-CuBDC after variation of the surface potential. Two models were constructed based on experimental observations, featuring Cu/Cu_2O NPs decorated onto the surface of the CuBDC (Figure S25). Finite-element simulations were employed by using the transport of diluted species modules.

Figure 4d,e illustrates the evolution of NO_3^- and H_2O concentrations in the Cu/Cu_2O model without the CuBDC support in the 3D simulation domain. It can be found that NO_3^- migrates away from the surface of Cu/Cu_2O while massive water molecules accumulate, which can raise the competitive HER and decrease the selectivity toward NITRR. In contrast, a substantial interface accumulation of NO_3^- is observed, whereas H_2O molecules are nearly excluded from the surface of Cu/Cu_2O with the presence of the CuBDC support (Figure 4f,g). To better monitor the diffusion processes, we tracked changes in the NO_3^- and H_2O concentrations around the catalyst surface of Cu/Cu_2O and E-CuBDC over time from 0 to 10 ps. As depicted in Figure 4h, the NO_3^- concentration rapidly decreases after 2 ps in the Cu/Cu_2O model, accompanied by a gradual increase in H_2O concentration. In sharp contrast, the NO_3^- concentration gradually increased, and the H_2O concentration declined on the E-CuBDC surface with time from 0 to 10 ps (Figures 4i and S26). All of these results illustrate that the Cu/Cu_2O-CuBDC interface in E-

https://doi.org/10.1021/jacs.5c00400
J. Am. Chem. Soc. 2025, 147, 21432−21442

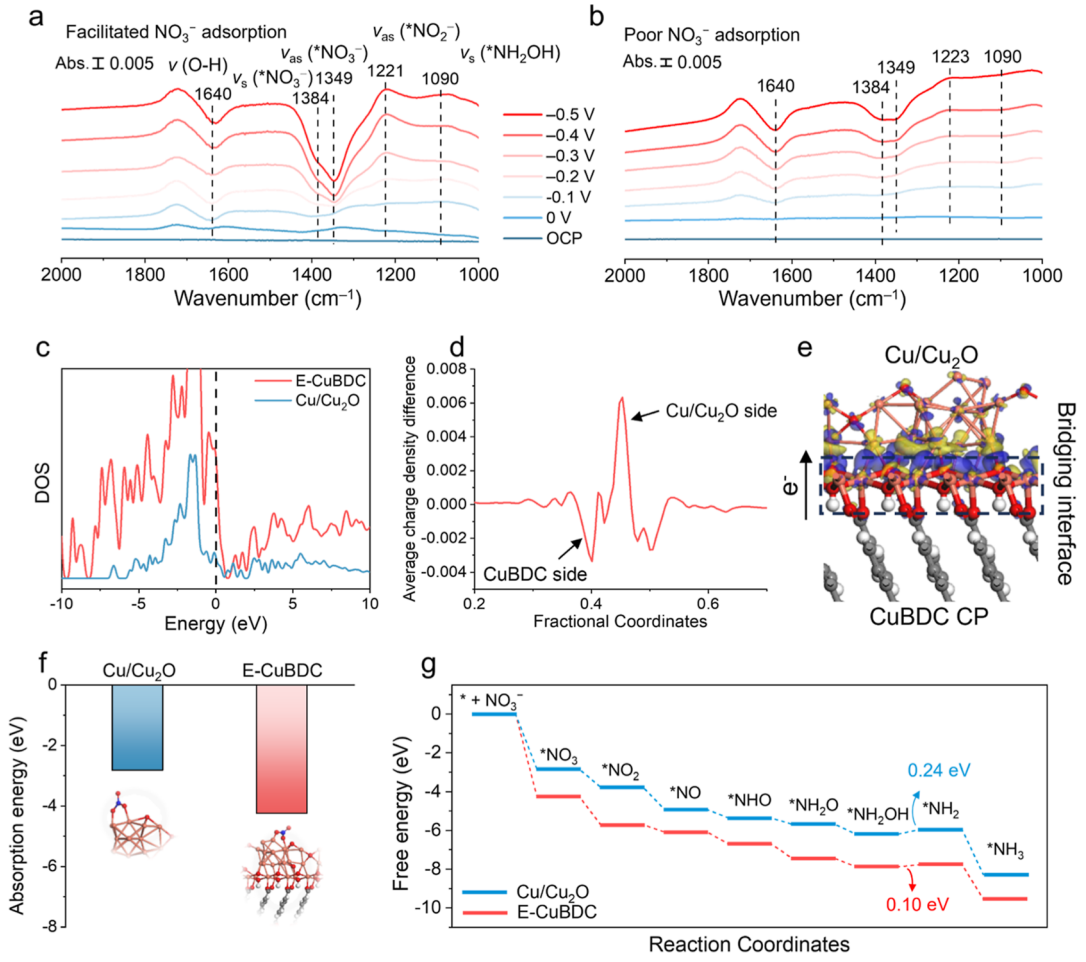

Figure 5. In situ ATR-SEIRAS characterization and density functional theory (DFT) calculations. (a,b) In situ ATR-SEIRAS spectra under NITRR operation for the E-CuBDC and Cu_2O catalysts, respectively. (c) Density of states (DOS) for the E-CuBDC and Cu/Cu_2O models. (d,e) Plane-averaged charge density difference at the Cu/Cu_2O-CuBDC bridging interface in the E-CuBDC model. (f) Calculated NO_3^- adsorption energies on the Cu/Cu_2O and E-CuBDC models. (g) Free-energy profiles of NITRR on the Cu/Cu_2O and E-CuBDC models with uphill energy barriers of 0.24 and 0.10 eV at the rate-determining step (*NH_2OH → *NH_2).

CuBDC creates a unique water-deficient and NO_3^--rich interface, suppressing the HER process and providing abundant unoccupied active sites for the NITRR process.

To gain mechanistic insights into how the metal−polymer interface regulates interfacial mass transport, we employed in situ attenuated total reflection surface-enhanced infrared absorption spectroscopy (ATR-SEIRAS). This technique also enables identification of reaction intermediates and provides information on the surface environment during the NITRR process. As shown in the ATR-SEIRAS spectra of E-CuBDC and Cu_2O (Figure 5a,b), the characteristic peak at 1384 and 1349 cm^{-1} is attributed to the N−O symmetric and asymmetric stretching vibration of *NO_3^-,[44] attributing to the consumption process of NO_3^-. The *NO_3^- peak of E-CuBDC declines much more than that of Cu_2O, indicating a higher concentration of *NO_3^- in the vicinity of E-CuBDC.

The upward band observed at around 1221 cm^{-1} is associated with the −N−O− antisymmetric stretching vibration of *NO_2^-,[45] implying the NO_2^- formation from the NO_3^- reduction. Upon the potential shifting negatively to −0.5 V, another upward absorption band emerges at around 1090 cm^{-1}, attributed to the stretching vibration of hydroxylamine (NH_2OH),[41,45] a crucial intermediate in NH_3 formation. The enhanced downward band at roughly 1640 cm^{-1} is linked to water electrolysis,[46] related to hydrogen production during the hydrodeoxidation of NO_3^-.[47] It deserves to note the start and enhancement of *NO_3^- band consumption on E-CuBDC at −0.1 V vs RHE, which were 200 mV more negative compared to pure Cu_2O. This indicates significantly increased adsorption of NO_3^- on the surface of E-CuBDC, aligning with the results obtained from molecular dynamics and finite-element simulations. Hence, the Janus metal−polymer interface in E-CuBDC facilitates the migration and accumulation of NO_3^-, leading to the formation of a NO_3^--rich domain near the catalyst surface. This provides a kinetically favorable local environment for the NITRR process. Besides, with the negative shift in working potentials, the band intensity of NO_2^- decreases, accompanied by an enhancement in the band intensity of NH_2OH generation, a distinction not observed with pure Cu_2O. The emergence of NH_2OH subsequent to NO_2^- formation, along with the rise in NH_2OH with the depletion of NO_2^-, implies that NH_2OH arises through the hydrogenation of NO_2^-. Further, we carried out in situ differential electrochemical mass spectrometry (DEMS) to detect potential intermediates (Figure S27). With the extension of time, signals corresponding to m/z 46, 30, 31, 33, 16, and 17 were observed, which can be attributed to the reaction intermediates of NO_2, NO, HNO, NH_2OH, NH_2, and

https://doi.org/10.1021/jacs.5c00400
J. Am. Chem. Soc. 2025, 147, 21432−21442

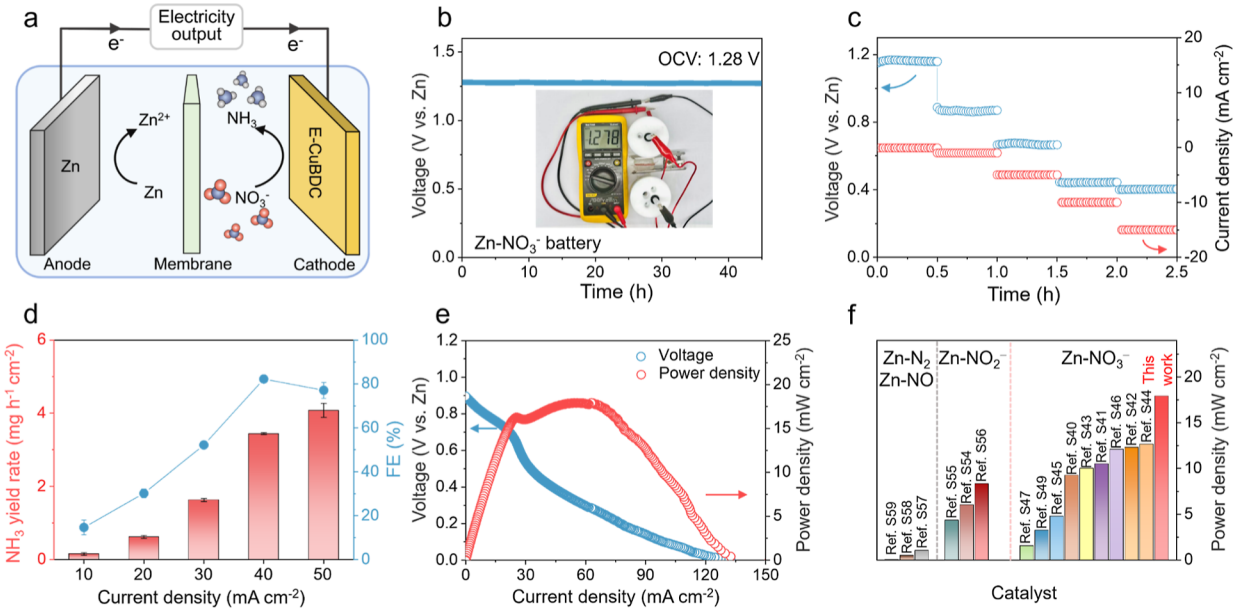

Figure 6. Zn−NO_3^- battery performance. (a) Schematic illustration of the Zn−NO_3^- battery assembled with the E-CuBDC cathode. (b) OCV curve of the Zn−NO_3^- battery assembled with the E-CuBDC cathode. Inset of (b) shows the photograph of the OCV measurement of the Zn−NO_3^- battery. (c) Rate capability of the Zn−NO_3^- battery at different discharge current densities. (d) NH_3 yield rate and FE of the Zn−NO_3^- battery at different current densities. (e) Discharge curve and power density of the Zn−NO_3^- battery. (f) Performance comparison between the Zn−NO_3^- battery with the E-CuBDC cathode and other reported Zn-nitrogen hybrid systems, including Zn−NO_3^-, Zn−NO_2^-, and Zn−N_2/NO batteries.

NH_3, respectively.[18] Combined with the in situ ATR-SEIRAS and DEMS, we proposed a possible route during the NITRR process on E-CuBDC: NO_3^- → *NO_3 → *NO_2 → *NO → *HNO → *NH_2OH → *NH_2 → *NH_3 (Figure S28).

Furthermore, DFT calculations were further conducted. First, we constructed simplified models of Cu/Cu_2O and E-CuBDC. As shown in Figure 5c, the DOS of E-CuBDC has a higher level near the Fermi level than that of Cu/Cu_2O at the Fermi level, suggesting promoted electron transfer to E-CuBDC. The charge density difference shown in Figure 5d,e shows that electrons transfer from the CuBDC substrate to Cu/Cu_2O, implying a negative and positive charge distribution on the Cu/Cu_2O and CuBDC substrate, respectively. The positive CuBDC substrate can form a boosted interfacial electric field, facilitating the absorption of anions such as NO_3^- or NO_2^- on the CuBDC surface. Moreover, the metal-centered Cu, featuring a less positive charge, functions as an electron reservoir capable of supplying and delivering electrons. The extra electrons localized near the Cu sites can greatly enhance the occupancy of the partially filled d-orbital, which can tailor the adsorption energy of NITRR intermediates, resulting in lowered energy barriers for intermediate formation. To further validate the above hypothesis, we introduced a NO_3^- onto the surfaces of E-CuBDC and Cu/Cu_2O (Figure 5f). The adsorption energy of NO_3^- on E-CuBDC (−4.24 eV) is lower than that on Cu/Cu_2O (−2.82 eV). This confirms a strong attractive effect of E-CuBDC for NO_3^-, thereby expediting the kinetics of NO_3^- transfer for subsequent reduction processes on Cu/Cu_2O, consistent with the findings of in situ ATR-SEIRAS. Based on the results offered by online DEMS and in situ ATR-SEIRAS, the NITRR process was investigated on E-CuBDC and Cu/Cu_2O, involving *NO_3, *NO_2, *NO, *NHO, *NH_2O, *NH_2OH, and *NH_2 intermediates, as depicted in Figures S29 and S30. From the corresponding Gibbs free-energy profile, we identified that the rate-determining step is step 7 (*NH_2OH → *NH_2), which shows a lower energy barrier of 0.10 eV compared to that of Cu/Cu_2O of 0.24 eV (Figure 5g). These theoretical calculations, taken together, suggest that the improved NITRR performance of E-CuBDC may arise from its accelerated reaction kinetics and thermodynamics.

Inspired by the superior performance of E-CuBDC for ammonia production, we proceeded to construct Zn−NO_3^- batteries using Zn plates as the anode and E-CuBDC as the cathode (Figure 6a), which presents great potential for sustainable ammonia synthesis and power generation.[48−53] As shown in Figure 6b, the open-circuit voltage (OCV) of the Zn−NO_3^- battery using the E-CuBDC cathode is approximately 1.28 V vs Zn. The OCV remains stable for over 45 h, highlighting the battery's ability to sustain a consistent voltage over an extended duration. During discharge, the anodic dissolution of Zn drives the NITRR at the E-CuBDC cathode. The Zn−NO_3^- battery exhibits a stable discharge profile characterized by a progressively decreasing potential coupled with a continuously increasing output current. This behavior remains consistent across measurements conducted at various discharge current densities, indicating its superior discharge performance (Figure 6c). To validate the Zn−NO_3^- battery as a dual-output system capable of producing valuable chemicals and electricity, the NH_3 yield rate and FE_{NH_3} were tested at increasing current densities (Figure 6d). Note that at current densities up to 40 mA cm^{-2}, the Zn−NO_3^- battery shows a high FE_{NH_3} of 82.2%, yielding a NH_3 yield rate of 3.4 mg h^{-1} cm^{-2}. The polarization profiles of the Zn−NO_3^- battery with an E-CuBDC cathode during discharging are presented (Figure 6e). The Zn−NO_3^- battery using the E-CuBDC cathode achieves a maximum power density of 17.9 mW cm^{-2}, exceeding those of Cu_2O (8.1 mW cm^{-2}) and Cu (5.4 mW cm^{-2}), as present in Figure S31. We also evaluated the long-

https://doi.org/10.1021/jacs.5c00400
J. Am. Chem. Soc. 2025, 147, 21432−21442

term stability of the Zn−NO_3^- battery employing the E-CuBDC cathode. As shown in Figure S32, the Zn−NO_3^- battery exhibits sustained voltage output for 140 h, underscoring the excellent stability of the system using the E-CuBDC cathode. In the realm of research for aqueous Zn-based batteries, this study stands out for its power density and durability, outperforming most reported Zn−nitrogen hybrid systems, including Zn−NO_3^-, Zn−NO_2^-, and Zn−N_2/NO batteries (Figure 6f and Table S3).

CONCLUSION

In summary, we design a metal−polymer composite with Cu/Cu_2O nanoparticles bridged on a 2D Cu-based benzene dicarboxylate by in situ electroreduction, which shows efficient and highly selective NH_3 synthesis from electrochemical nitrate (NO_3^-) reduction reaction. Electrochemical reduction of NO_3^- to NH_3, instead of N_2, enhances the economic and practical value of the process. NH_3 serves as a crucial nitrogen source for agricultural fertilizers, a key chemical feedstock for various industrial applications, and a high-energy-density carrier for renewable hydrogen storage and utilization. The optimal E-CuBDC exhibits a FE_{NH_3} of 96.6% with a NH_3 yield rate of 15.7 mg h^{-1} cm^{-2} at −0.65 V vs RHE. More significantly, E-CuBDC achieves high FE_{NH_3} over 90% across wide NO_3^- concentrations (100−1400 NO_3^--N mg L^{-1}) and under high applied voltages. It maintains stable NH_3 production over 100 h at around 1.2 A cm^{-2}. The ATR-SEIRAS, finite-element simulations, and DFT calculations confirm that the constructed Cu/Cu_2O-CuBDC Janus interface can induce synergistic modulation of facilitating the mass accumulation of NO_3^- and restricting H_2O accessibility at the electrode surface. Further, as demonstrated, the Zn−NO_3^- battery using E-CuBDC as a cathode simultaneously generates electricity and produce NH_3, with a power density of 17.9 mW cm^{-2} and a FE_{NH_3} of 82.2%. This study highlights an effective methodology of constructing high-performance catalysts with metal−polymer interfaces in efficient NH_3 synthesis from NO_3^- reduction electrocatalysis and Zn-based hybrid electrochemical energy storage systems.

ASSOCIATED CONTENT

Supporting Information

The Supporting Information is available free of charge at https://pubs.acs.org/doi/10.1021/jacs.5c00400.

Detailed experimental procedures, characterizations, computational methods, FTIR spectra, XRD patterns, TEM images, low- and high-magnification TEM images, high-angle annular dark-field scanning TEM image, Raman spectra, LSV curves, Tafel slopes, *i*−*t* curves, surface zeta potential, DEMS measurements (PDF)

AUTHOR INFORMATION

Corresponding Authors

Wei Zong − *Department of Engineering Science, University of Oxford, Oxford OX1 3PJ, U.K.; Christopher Ingold Laboratory, Department of Chemistry, University College London, London WC1H 0AJ, U.K.;* orcid.org/0000-0002-1815-6471; Email: wei.zong@eng.ox.ac.uk

Longsheng Zhang − *Key Laboratory of Synthetic and Biological Colloids, Ministry of Education, School of Chemical and Material Engineering, International Joint Research Laboratory for Nano Energy Composites, Jiangnan University, Wuxi 214122, P. R. China;* orcid.org/0000-0002-0241-4237; Email: zhangls@jiangnan.edu.cn

Guanjie He − *Christopher Ingold Laboratory, Department of Chemistry, University College London, London WC1H 0AJ, U.K.;* orcid.org/0000-0002-7365-9645; Email: g.he@ucl.ac.uk

Tianxi Liu − *Key Laboratory of Synthetic and Biological Colloids, Ministry of Education, School of Chemical and Material Engineering, International Joint Research Laboratory for Nano Energy Composites, Jiangnan University, Wuxi 214122, P. R. China*; Email: txliu@jiangnan.edu.cn

Authors

Guojie Chao − *Key Laboratory of Synthetic and Biological Colloids, Ministry of Education, School of Chemical and Material Engineering, International Joint Research Laboratory for Nano Energy Composites, Jiangnan University, Wuxi 214122, P. R. China*

Jiexin Zhu − *Department of Mechanical and Industrial Engineering, University of Toronto, Toronto, Ontario M5S 3G8, Canada;* orcid.org/0000-0003-1629-240X

Haifeng Wang − *State Key Laboratory for Modification of Chemical Fibers and Polymer Materials & College of Materials Science and Engineering, Donghua University, Shanghai 201620, China*

Kaibin Chu − *Key Laboratory of Synthetic and Biological Colloids, Ministry of Education, School of Chemical and Material Engineering, International Joint Research Laboratory for Nano Energy Composites, Jiangnan University, Wuxi 214122, P. R. China*

Hele Guo − *Key Laboratory of Synthetic and Biological Colloids, Ministry of Education, School of Chemical and Material Engineering, International Joint Research Laboratory for Nano Energy Composites, Jiangnan University, Wuxi 214122, P. R. China*

Jian Wang − *Key Laboratory of Synthetic and Biological Colloids, Ministry of Education, School of Chemical and Material Engineering, International Joint Research Laboratory for Nano Energy Composites, Jiangnan University, Wuxi 214122, P. R. China*

Yuhang Dai − *Department of Engineering Science, University of Oxford, Oxford OX1 3PJ, U.K.*

Xuan Gao − *Department of Engineering Science, University of Oxford, Oxford OX1 3PJ, U.K.;* orcid.org/0000-0003-1706-3801

Longxiang Liu − *Christopher Ingold Laboratory, Department of Chemistry, University College London, London WC1H 0AJ, U.K.*

Fei Guo − *Christopher Ingold Laboratory, Department of Chemistry, University College London, London WC1H 0AJ, U.K.*

Ivan P. Parkin − *Christopher Ingold Laboratory, Department of Chemistry, University College London, London WC1H 0AJ, U.K.;* orcid.org/0000-0002-4072-6610

Wei Luo − *State Key Laboratory for Modification of Chemical Fibers and Polymer Materials & College of Materials Science and Engineering, Donghua University, Shanghai 201620, China;* orcid.org/0000-0001-6126-899X

Paul R. Shearing − *Department of Engineering Science, University of Oxford, Oxford OX1 3PJ, U.K.;* orcid.org/0000-0002-1387-9531

Complete contact information is available at:
https://pubs.acs.org/10.1021/jacs.5c00400

Author Contributions

#G.C., W.Z., J.Z., and H.W. contributed equally to this work.

Notes

The authors declare no competing financial interest.

■ ACKNOWLEDGMENTS

This work was supported by the National Natural Science Foundation of China (52303342, 52373211, 52211530489, 52161135302) and the Natural Science Foundation of Jiangsu Province (BK20221099, BK20210482), the Engineering and Physical Sciences Research Council (EPSRC, EP/V027433/3), the UK Research and Innovation (UKRI) under the UK Government's Horizon Europe funding (101077226; EP/Y008707/1), the Royal Society (IES\R2\212115; IEC\NSFC\211019), and the EPSRC Centre for Doctoral Training in Molecular Modelling and Materials Science (EP/L015862/1). We thank Beamline BL11B at the Shanghai Synchrotron Radiation Facility for XAFS measurement..

■ REFERENCES

(1) Good, A. Toward nitrogen-fixing plants. *Science* **2018**, *359* (6378), 869−870.
(2) Ghosh, M.; Braley, S. E.; Ezhov, R.; Worster, H.; Valdez-Moreira, J. A.; Losovyj, Y.; Jakubikova, E.; Pushkar, Y. N.; Smith, J. M. A spectroscopically observed iron nitrosyl intermediate in the reduction of nitrate by a surface-conjugated electrocatalyst. *J. Am. Chem. Soc.* **2022**, *144* (39), 17824−17831.
(3) Gruber, N.; Galloway, J. N. An Earth-system perspective of the global nitrogen cycle. *Nature* **2008**, *451* (7176), 293−296.
(4) Rosca, V.; Duca, M.; de Groot, M. T.; Koper, M. T. Nitrogen cycle electrocatalysis. *Chem. Rev.* **2009**, *109* (6), 2209−2244.
(5) Qing, G.; Ghazfar, R.; Jackowski, S. T.; Habibzadeh, F.; Ashtiani, M. M.; Chen, C.-P.; Smith, M. R., III; Hamann, T. W. Recent advances and challenges of electrocatalytic N_2 reduction to ammonia. *Chem. Rev.* **2020**, *120* (12), 5437−5516.
(6) Chen, G.-F.; Yuan, Y.; Jiang, H.; Ren, S.-Y.; Ding, L.-X.; Ma, L.; Wu, T.; Lu, J.; Wang, H. Electrochemical reduction of nitrate to ammonia via direct eight-electron transfer using a copper−molecular solid catalyst. *Nat. Energy* **2020**, *5* (8), 605−613.
(7) Andersen, S. Z.; Colić, V.; Yang, S.; Schwalbe, J. A.; Nielander, A. C.; McEnaney, J. M.; Enemark-Rasmussen, K.; Baker, J. G.; Singh, A. R.; Rohr, B. A. J. N.; et al. A rigorous electrochemical ammonia synthesis protocol with quantitative isotope measurements. *Nature* **2019**, *570* (7762), 504−508.
(8) Han, G.-F.; Li, F.; Chen, Z.-W.; Coppex, C.; Kim, S.-J.; Noh, H.-J.; Fu, Z.; Lu, Y.; Singh, C. V.; Siahrostami, S.; et al. Mechanochemistry for ammonia synthesis under mild conditions. *Nat. Nanotechnol.* **2021**, *16* (3), 325−330.
(9) Service, R. F. New recipe produces ammonia from air, water, and sunlight. *Science* **2014**, *345* (6197), 610.
(10) Chu, K.; Zong, W.; Xue, G.; Guo, H.; Qin, J.; Zhu, H.; Zhang, N.; Tian, Z.; Dong, H.; Miao, Y. E.; Roeffaers, M. B. J.; Hofkens, J.; Lai, F.; Liu, T. Cation substitution strategy for developing perovskite oxide with rich oxygen vacancy-mediated charge redistribution enables highly efficient nitrate electroreduction to ammonia. *J. Am. Chem. Soc.* **2023**, *145* (39), 21387−21396.
(11) Katsounaros, I.; Dortsiou, M.; Kyriacou, G. Electrochemical reduction of nitrate and nitrite in simulated liquid nuclear wastes. *J. Hazard. Mater.* **2009**, *171* (1−3), 323−327.
(12) Chen, W.; Yang, X.; Huang, T.; Li, Y.; Ren, X.; Ye, S.; Zhang, Q.; Liu, J. Constructing flexible composite electrodes of low crystalline cobalt (Oxy) hydroxides nanosheet grown on carbon fiber cloth via self-reconstruction for electrochemical nitrate-to-ammonia conversion. *Compos. Commun.* **2023**, *43*, 101715.
(13) Wang, K.; Mao, R.; Liu, R.; Zhang, J.; Zhao, H.; Ran, W.; Zhao, X. Intentional corrosion-induced reconstruction of defective NiFe layered double hydroxide boosts electrocatalytic nitrate reduction to ammonia. *Nat. Water* **2023**, *1* (12), 1068−1078.
(14) Wang, Y.; Xu, A.; Wang, Z.; Huang, L.; Li, J.; Li, F.; Wicks, J.; Luo, M.; Nam, D.-H.; Tan, C.-S.; et al. Enhanced nitrate-to-ammonia activity on copper−nickel alloys via tuning of intermediate adsorption. *J. Am. Chem. Soc.* **2020**, *142* (12), 5702−5708.
(15) Murphy, A. P. Chemical removal of nitrate from water. *Nature* **1991**, *350* (6315), 223−225.
(16) Han, S.; Li, H.; Li, T.; Chen, F.; Yang, R.; Yu, Y.; Zhang, B. Ultralow overpotential nitrate reduction to ammonia via a three-step relay mechanism. *Nat. Catal.* **2023**, *6* (5), 402−414.
(17) Guo, Y.; Zhang, R.; Zhang, S.; Zhao, Y.; Yang, Q.; Huang, Z.; Dong, B.; Zhi, C. Pd doping-weakened intermediate adsorption to promote electrocatalytic nitrate reduction on TiO_2 nanoarrays for ammonia production and energy supply with zinc−nitrate batteries. *Energy Environ. Sci.* **2021**, *14* (7), 3938−3944.
(18) Wang, Y.; Zhou, W.; Jia, R.; Yu, Y.; Zhang, B. Unveiling the activity origin of a copper-based electrocatalyst for selective nitrate reduction to ammonia. *Angew. Chem., Int. Ed.* **2020**, *59* (13), 5350−5354.
(19) He, W.; Zhang, J.; Dieckhöfer, S.; Varhade, S.; Brix, A. C.; Lielpetere, A.; Seisel, S.; Junqueira, J. R. C.; Schuhmann, W. Splicing the active phases of copper/cobalt-based catalysts achieves high-rate tandem electroreduction of nitrate to ammonia. *Nat. Commun.* **2022**, *13* (1), 1129.
(20) Li, P.; Li, R.; Liu, Y.; Xie, M.; Jin, Z.; Yu, G. Pulsed nitrate-to-ammonia electroreduction facilitated by tandem catalysis of nitrite intermediates. *J. Am. Chem. Soc.* **2023**, *145* (11), 6471−6479.
(21) Cui, Y.; Sun, C.; Ding, G.; Zhao, M.; Ge, X.; Zhang, W.; Zhu, Y.; Wang, Z.; Jiang, Q. Synergistically tuning intermediate adsorption and promoting water dissociation to facilitate electrocatalytic nitrate reduction to ammonia over nanoporous Ru-doped Cu catalyst. *Sci. China Mater.* **2023**, *66* (11), 4387−4395.
(22) Kim, K.; Zagalskaya, A.; Ng, J. L.; Hong, J.; Alexandrov, V.; Pham, T. A.; Su, X. Coupling nitrate capture with ammonia production through bifunctional redox-electrodes. *Nat. Commun.* **2023**, *14* (1), 823.
(23) Liu, C.; Zhang, G.; Zhang, W.; Gu, Z.; Zhu, G. Specifically adsorbed ferrous ions modulate interfacial affinity for high-rate ammonia electrosynthesis from nitrate in neutral media. *Proc. Natl. Acad. Sci. U.S.A.* **2023**, *120* (3), No. e2209979120.
(24) Bard, A. J.; Faulkner, L. R.; White, H. S. *Electrochemical Methods: Fundamentals and Applications*; John Wiley & Sons, 2001.
(25) Zong, W.; Gao, H.; Ouyang, Y.; Chu, K.; Guo, H.; Zhang, L.; Zhang, W.; Chen, R.; Dai, Y.; Guo, F.; Zhu, J.; Zhang, Z.; Ye, C.; Miao, Y.-E.; Hofkens, J.; Lai, F.; Liu, T. Bio-inspired aerobic-hydrophobic Janus interface on partially carbonized iron hetero-structure promotes bifunctional nitrogen fixation. *Angew. Chem., Int. Ed.* **2023**, *62*, No. e202218122.
(26) Duca, M.; Koper, M. T. M. Powering denitrification: the perspectives of electrocatalytic nitrate reduction. *Energy Environ. Sci.* **2012**, *5* (12), 9726−9742.
(27) Wang, Y.; Kang, Y.; Miao, Y.; Jia, M.; Long, S.; Diao, L.; Zhang, L.; Li, D.; Wu, G. S-dopant and O-vacancy of mesoporous ZnO nanosheets induce high efficiency and selectivity of electrocatalytic CO_2 reduction to CO. *Compos. Commun.* **2024**, *48*, 101890.
(28) Hu, Q.; Qi, S.; Huo, Q.; Zhao, Y.; Sun, J.; Chen, X.; Lv, M.; Zhou, W.; Feng, C.; Chai, X.; et al. Designing efficient nitrate reduction electrocatalysts by identifying and optimizing active sites of Co-based spinels. *J. Am. Chem. Soc.* **2023**, *146* (5), 2967−2976.
(29) Ba, J.; Dong, H.; Odziomek, M.; Lai, F.; Wang, R.; Han, Y.; Shu, J.; Antonietti, M.; Liu, T.; Yang, W.; Tian, Z. Red carbon mediated formation of Cu_2O clusters dispersed on the oxocarbon framework by Fehling's route and their use for the nitrate

electroreduction in acidic conditions. *Adv. Mater.* **2024**, *36*, No. e2400396.
(30) Zhu, J.; Xia, L.; Yu, R.; Lu, R.; Li, J.; He, R.; Wu, Y.; Zhang, W.; Hong, X.; Chen, W.; et al. Ultrahigh stable methanol oxidation enabled by a high hydroxyl concentration on Pt clusters/MXene interfaces. *J. Am. Chem. Soc.* **2022**, *144* (34), 15529−15538.
(31) Chen, R.; Cheng, L.; Liu, J.; Wang, Y.; Ge, W.; Xiao, C.; Jiang, H.; Li, Y.; Li, C. Toward high-performance CO_2-to-C_2 electroreduction via linker tuning on MOF-derived catalysts. *Small* **2022**, *18* (18), 2200720.
(32) Zhan, G.; Fan, L.; Zhao, F.; Huang, Z.; Chen, B.; Yang, X.; Zhou, S. f. Fabrication of ultrathin 2D Cu-BDC nanosheets and the derived integrated MOF nanocomposites. *Adv. Funct. Mater.* **2019**, *29* (9), 1806720.
(33) Rodenas, T.; Luz, I.; Prieto, G.; Seoane, B.; Miro, H.; Corma, A.; Kapteijn, F.; Llabrés i Xamena, F. X.; Gascon, J. Metal−organic framework nanosheets in polymer composite materials for gas separation. *Nat. Mater.* **2015**, *14* (1), 48−55.
(34) Yu, Z.; Zhao, W.; Mu, M.; Chen, G.; Yu, W.; Liu, X. Highly thermal conductive epoxy composites enabled by 3D graphene/Cu-based dual networks for efficient thermal management. *Compos. Commun.* **2024**, *46*, 101845.
(35) Martin, L.; Martinez, H.; Poinot, D.; Pecquenard, B.; Le Cras, F. Comprehensive X-ray photoelectron spectroscopy study of the conversion reaction mechanism of CuO in lithiated thin film electrodes. *J. Phys. Chem. C* **2013**, *117* (9), 4421−4430.
(36) Wang, M.; Chen, H.; Wang, M.; Wang, J.; Tuo, Y.; Li, W.; Zhou, S.; Kong, L.; Liu, G.; Jiang, L.; Wang, G. Tuning C_1/C_2 selectivity of CO_2 electrochemical reduction over in-situ evolved CuO/SnO_2 heterostructure. *Angew. Chem., Int. Ed.* **2023**, *62* (40), No. e202306456.
(37) Wang, C.; Sun, N.; Xu, W.; Liu, L.; Ding, H.; He, H.; Ding, C.; Yang, W.; Xing, W.; Yu, B. Staggered distribution structure Cu-Mn catalysts for mitigating smoke and gas toxicity in combustion: unravelling mechanistic insight through operando studies. *Compos. Commun.* **2024**, *52*, 102142.
(38) Bai, L.; Franco, F.; Timoshenko, J.; Rettenmaier, C.; Scholten, F.; Jeon, H. S.; Yoon, A.; Rüscher, M.; Herzog, A.; Haase, F. T.; et al. Electrocatalytic nitrate and nitrite reduction toward ammonia using Cu_2O nanocubes: active species and reaction mechanisms. *J. Am. Chem. Soc.* **2024**, *146* (14), 9665−9678.
(39) Zhu, G.; Bao, W.; Xie, M.; Qi, C.; Xu, F.; Jiang, Y.; Chen, B.; Fan, Y.; Liu, B.; Wang, L.; Jiang, W.; Qiu, P.; Luo, W. Accelerating tandem electroreduction of nitrate to ammonia via multi-site synergy in mesoporous carbon-supported high-entropy intermetallics. *Adv. Mater.* **2025**, *37* (5), No. e2413560.
(40) Shih, Y.-J.; Hsu, C.-H. Kinetics and highly selective N_2 conversion of direct electrochemical ammonia oxidation in an undivided cell using NiCo oxide nanoparticle as the anode and metallic Cu/Ni foam as the cathode. *Chem. Eng. J.* **2021**, *409*, 128024.
(41) Fang, J.-Y.; Zheng, Q.-Z.; Lou, Y.-Y.; Zhao, K.-M.; Hu, S.-N.; Li, G.; Akdim, O.; Huang, X.-Y.; Sun, S.-G. Ampere-level current density ammonia electrochemical synthesis using CuCo nanosheets simulating nitrite reductase bifunctional nature. *Nat. Commun.* **2022**, *13* (1), 7899.
(42) Zhu, T.; Chen, Q.; Liao, P.; Duan, W.; Liang, S.; Yan, Z.; Feng, C. Single-atom Cu catalysts for enhanced electrocatalytic nitrate reduction with significant alleviation of nitrite production. *Small* **2020**, *16* (49), 2004526.
(43) Chen, X.; Cheng, Y.; Zhang, B.; Zhou, J.; He, S. Gradient-concentration RuCo electrocatalyst for efficient and stable electroreduction of nitrate into ammonia. *Nat. Commun.* **2024**, *15* (1), 6278.
(44) Figueiredo, M. C.; Souza-Garcia, J.; Climent, V.; Feliu, J. M. Nitrate reduction on Pt (111) surfaces modified by Bi adatoms. *Electrochem. Commun.* **2009**, *11* (9), 1760−1763.
(45) Pérez-Gallent, E.; Figueiredo, M. C.; Katsounaros, I.; Koper, M. T. M. Electrocatalytic reduction of nitrate on copper single crystals in acidic and alkaline solutions. *Electrochim. Acta* **2017**, *227*, 77−84.
(46) Ataka, K.-i.; Yotsuyanagi, T.; Osawa, M. Potential-dependent reorientation of water molecules at an electrode/electrolyte interface studied by surface-enhanced infrared absorption spectroscopy. *J. Phys. Chem.* **1996**, *100* (25), 10664−10672.
(47) Rosca, V.; Beltramo, G. L.; Koper, M. T. M. Hydroxylamine electrochemistry at polycrystalline platinum in acidic media: a voltammetric, DEMS and FTIR study. *Electrochem. Commun.* **2004**, *566* (1), 53−62.
(48) Ouyang, Y.; Zong, W.; Gao, X.; Leong, S. X.; Chen, J. R. T.; Dai, Y.; Dong, H.; Phang, I. Y.; Shearing, P. R.; He, G.; Miao, Y.-E.; Liu, T.; Ling, X. Y. Regulating interfacial molecular configuration to drive facet-selective Zn metal deposition. *Angew. Chem., Int. Ed.* **2025**, No. e202504965.
(49) Zhang, S.; Yang, L.; Yang, T.; Song, Y.; Jia, M.; Yang, J.; Liu, Y.; Zhou, X.; Tang, J. Pomegranate-like structured FeNi-nanodots@FeNi LDH composite as a high performance bifunctional catalyst for oxygen electrocatalytic reactions in zinc-air batteries. *Compos. Commun.* **2023**, *44*, 101757.
(50) Xu, H.; Ma, Y.; Chen, J.; Zhang, W.-x.; Yang, J. Electrocatalytic reduction of nitrate−a step towards a sustainable nitrogen cycle. *Chem. Soc. Rev.* **2022**, *51* (7), 2710−2758.
(51) Xie, M.; Tang, S.; Li, Z.; Wang, M.; Jin, Z.; Li, P.; Zhan, X.; Zhou, H.; Yu, G. Intermetallic single-atom alloy In−Pd bimetallene for neutral electrosynthesis of ammonia from nitrate. *J. Am. Chem. Soc.* **2023**, *145* (25), 13957−13967.
(52) Zong, W.; Li, J.; Zhang, C.; Dai, Y.; Ouyang, Y.; Zhang, L.; Li, J.; Zhang, W.; Chen, R.; Dong, H.; Gao, X.; Zhu, J.; Parkin, I. P.; Shearing, P. R.; Lai, F.; Amine, K.; Liu, T.; He, G. Dynamical Janus interface design for reversible and fast-charging zinc−iodine battery under extreme operating conditions. *J. Am. Chem. Soc.* **2024**, *146* (31), 21377−21388.
(53) Zhang, R.; Hong, H.; Liu, X.; Zhang, S.; Li, C.; Cui, H.; Wang, Y.; Liu, J.; Hou, Y.; Li, P.; et al. Molecular engineering of a metal-organic polymer for enhanced electrochemical nitrate-to-ammonia conversion and zinc nitrate batteries. *Angew. Chem., Int. Ed.* **2023**, *62* (48), No. e202309930.

https://doi.org/10.1021/jacs.5c00400
J. Am. Chem. Soc. 2025, 147, 21432−21442